

Singular Value-based Atmospheric Tomography with Fourier Domain Regularization (SAFR)

Lukas Weissinger* Simon Hubmer[†] Bernadett Stadler*
Ronny Ramlau*[†]

October 23, 2025

Abstract

Atmospheric tomography, the problem of reconstructing atmospheric turbulence profiles from wavefront sensor measurements, is an integral part of many adaptive optics systems. It is used to enhance the image quality of ground-based telescopes, such as for the Multiconjugate Adaptive Optics Relay For ELT Observations (MORFEO) instrument on the Extremely Large Telescope (ELT). To solve this problem, a singular-value decomposition (SVD) based approach has been proposed in [31]. In this paper, we focus on the numerical implementation of the SVD-based Atmospheric Tomography with Fourier Domain Regularization Algorithm (SAFR) and its performance for Multi-Conjugate Adaptive Optics (MCAO) systems. The key features of the SAFR algorithm are the utilization of the FFT and the pre-computation of computationally demanding parts. Together, this yields a fast algorithm with less memory requirements than commonly used Matrix Vector Multiplication (MVM) approaches. We evaluate the performance of SAFR regarding reconstruction quality and computational expense in numerical experiments using the simulation environment COMPASS, in which we use an MCAO setup resembling the physical parameters of the MORFEO instrument of the ELT.

Keywords. Atmospheric Tomography, Singular Value Decomposition, Adaptive Optics, Multiconjugate Adaptive Optics Relay, Extremely Large Telescope (ELT)

1 Introduction

The image quality of ground-based telescopes suffers from temperature fluctuations in the atmosphere, which results in wavefront aberrations of the incoming light.

*Johann Radon Institute Linz, Altenbergerstraße 69, A-4040 Linz, Austria, (lukas.weissinger@ricam.oeaw.ac.at, bernadett.stadler@ricam.oeaw.ac.at, ronny.ramlau@ricam.oeaw.ac.at).

[†]Johannes Kepler University Linz, Institute of Industrial Mathematics, Altenbergerstraße 69, A-4040 Linz, Austria, (simon.hubmer@jku.at, ronny.ramlau@jku.at).

These aberrations are typically corrected by an Adaptive Optics (AO) system to prevent an otherwise severe loss of image quality. Multi Conjugate Adaptive Optics (MCAO) systems, such as the MORFEO instrument of the ELT, aim for an aberration correction over a large field of view. For this, several wavefront sensors (WFSs) are used to estimate the resulting wavefront aberrations and correct for them using deformable mirrors (DMs) [41]. The WFSs use the incoming light from either natural guide stars (NGS) or artificial laser guide stars (LGS), which are created by powerful lasers in the sodium layer of the atmosphere, that act as reference objects.

The calculation of optimal mirror shapes for the DMs is commonly done by inverting the so called interaction matrix. This matrix relates DM commands to WFS measurements. The multiplication of the WFS measurements with this inverse matrix is often referred to as the Matrix Vector Multiplication (MVM) method. Since the atmosphere changes rapidly, the mirror shapes have to be updated at a rate of about 500-1000 Hz. To meet this strict time requirements, MVM methods can leverage parallel computations. However, the computational demand of a matrix vector multiplication of $\mathcal{O}(N^2)$, where N denotes the number of sensor measurements, is still high. Therefore, as telescope sizes increase, the demand for efficient algorithms has grown as well. Hence, as an alternative to MVM methods, three-step approaches [46] have been proposed, where the full AO-task is split into the 3 sub-problems:

1. **Wavefront reconstruction** from wavefront sensor measurements.
2. **Reconstruction of atmospheric turbulence** from wavefronts.
3. **Computation of deformable mirror shapes** from turbulence layers.

For solving the first of these sub-problems, different wavefront reconstruction methods have been proposed [21, 33, 34, 49, 55, 58]. For the numerical experiments considered in Section 4, we use the Cumulative Reconstructor with Domain Decomposition (CuReD) [43, 44], a reliable and efficient method scaling at $\mathcal{O}(N)$.

In this paper, we focus on the second sub-problem of the atmospheric tomography problem, i.e., the reconstruction of the turbulence volume above the telescope from the reconstructed wavefronts. Atmospheric tomography is a *limited-angle* tomography problem, since only a small number of guide stars with a small angle of separation are available. As such, it is severely ill-posed and thus practically infeasible to solve without additional restrictions [2, 30, 40]. Hence, one commonly assumes that the atmosphere consists of a finite number of (infinitely) thin turbulent layers located at predefined heights, and aims to reconstruct this layered atmospheric turbulence profile. An example of this problem for the case of three layers and three (natural) guide stars with corresponding WFSs is shown in Figure 1.1 (left).

The third sub-problem is usually referred to as mirror fitting and can be solved using, e.g., Kaczmarz iteration [45] or the CG method [14, 62]. However, this step can be omitted if the layer heights are chosen such that the light emitted from a certain turbulent layer is exactly focused in the corresponding DM. This special choice of the mirror position along the optical axis is typically referred to as

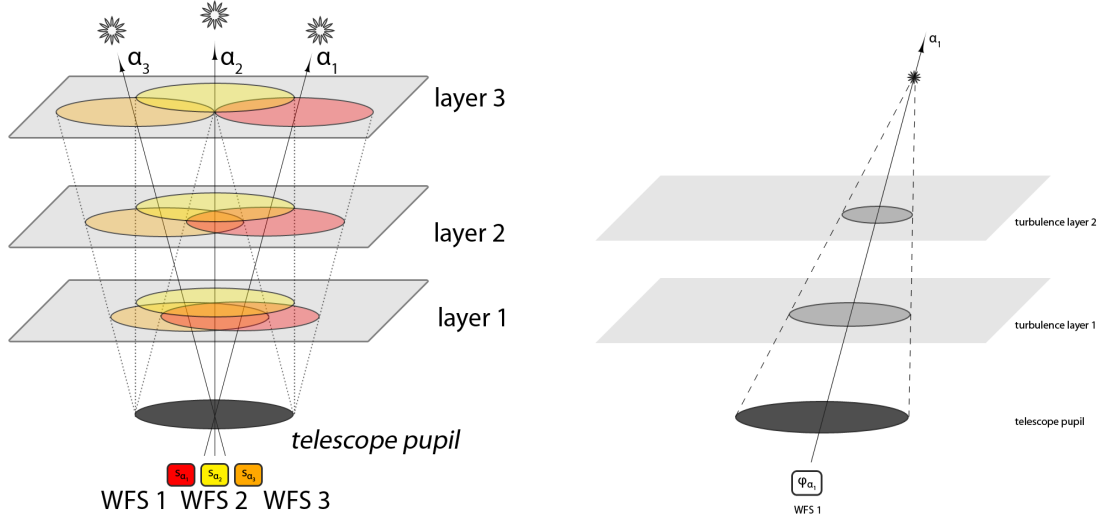


Figure 1.1: Illustration of the atmospheric tomography problem with three turbulence layers, NGSs and corresponding WFSs (left). Light stemming from a single LGS is influenced by the cone effect (right). Images taken from [62].

conjugation and allows the DM shapes to be obtained directly from the reconstructed layers.

The atmospheric tomography problem has attracted considerable attention in the past. Among the many proposed reconstruction methods we mention the minimum mean square error method [14], conjugate gradient type iterative reconstruction methods with suitable preconditioning [7, 17, 20, 57, 61], Fourier transform-based methods [56, 15], the Fractal Iterative Method (FrIM) [53, 54, 55], the Finite Element Wavelet Hybrid Algorithm (FEWHA) [50, 51, 62, 63, 64], as well as a Kaczmarz iteration [37, 45]. For further methods as well as important practical considerations see also [6, 18, 19, 32, 35, 36, 47] and the references therein. FEWHA is an iterative reconstruction algorithm which uses a dual-domain discretization strategy into wavelet and bilinear basis functions leading to sparse operators. A matrix-free representation of all involved operators makes FEWHA very fast and enables on-the-fly system updates whenever parameters at the telescope or in the atmosphere change [50, 51]. The resulting sparse system is solved using the CG method with a Jacobi preconditioner [63] and an augmented Krylov subspace method [50, 51]. We use FEWHA as a benchmark algorithm, since it has been shown that it leads to an excellent reconstruction quality compared to standard MVM approaches for the MORFEO instrument, while also being computationally efficient [50, 52].

To provide theoretical insights into the ill-posedness of the atmospheric tomography problem, a singular value decomposition (SVD) has been proposed in [31]. This SVD has only been derived for square telescope apertures in an NGS-only setting, which limits its practical applicability. In [23], the SVD has been extended to an LGS-only setting. Moreover, a frame-decomposition was proposed, which provides an SVD-like decomposition of the atmospheric tomography operator allowing for general aperture shapes and a mixture of NGS and LGS. The main drawback of

the frame-decomposition is that it only provides an approximate solution to the atmospheric tomography problem; cf. [24, 59, 60]. Finally, in [60], the SVD of the atmospheric tomography operator was further extended to incorporate atmosphere statistics, which formed the basis of the SAFR algorithm (called SVTD in [60]).

Motivated by the excellent performance of the SAFR algorithm in [60], in this paper we particularly study SAFR in the context of a three-step method for MCAO systems. We give a detailed description of the algorithm and conduct a performance analysis for the MORFEO instrument using the simulation environment COMPASS [12]. Moreover, we provide a detailed study of the quality as well as the computational complexity of SAFR, and propose a strategy to overcome the limitation that the classic SVD-approach can only be used in an LGS or NGS-only setting.

The paper is organized as follows: The atmospheric tomography problem and the related operator are defined in Section 2. Then, we recall the SVD as a method to solve the atmospheric tomography problem and derive the SAFR algorithm in Section 3. The quality and computational performance of the algorithm within an AO system compared against FEWHA and an MVM-like method is demonstrated by numerical simulations in Section 4. In Section 5, we present our final conclusions.

2 Atmospheric Tomography in Three-step Adaptive Optics

In this section, we introduce the mathematical formulation of the atmospheric tomography problem using a layered structure of the turbulence [5, 14]. Let h_{LGS} denote the height of the sodium layer in the atmosphere in which LGSs are created (approximately 90 km). We assume that there are L atmospheric layers, i.e., planes parallel to the telescope aperture Ω_A , located at distinct heights $h_\ell \in [0, h_{\text{LGS}})$ for $\ell = 1, \dots, L$. The heights are assumed to be in ascending order. We consider G different guide stars with corresponding direction vectors $\alpha_g = (\alpha_g^x, \alpha_g^y) \in \mathbb{R}^2$ for $g = 1, \dots, G$. The vectors α_g are chosen such that, seen from the center of the telescope aperture, the vectors $(\alpha_g^x, \alpha_g^y, 1) \in \mathbb{R}^3$ point at the corresponding guide stars. Here, we consider the NGS-only or LGS-only case and correspondingly define

$$c_\ell := \begin{cases} 1, & \text{NGS-only setting,} \\ 1 - h_\ell/h_{\text{LGS}}, & \text{LGS-only setting.} \end{cases}$$

The coefficients c_ℓ model the cone effect for LGS as illustrated in Figure 1.1 (right). Note that since $h_\ell < h_{\text{LGS}}$ for all $\ell = 1, \dots, L$, we have $c_\ell \in (0, 1]$.

Furthermore, we define the square domain $\Omega_T = [-T, T]^2 \subset \mathbb{R}^2$, with T chosen sufficiently large, such that

$$\Omega_A + \alpha_g h_\ell \subset c_\ell \Omega_T, \quad \forall g = 1, \dots, G, \quad \forall \ell = 1, \dots, L,$$

where $c_\ell \Omega_T := [c_\ell T, c_\ell T]^2$. For the incoming wavefronts $\varphi = (\varphi_g)_{g=1, \dots, G}$ we assume that $\varphi_g \in L^2(\Omega_T)$ and that they are (component-wise) periodic. To incorporate atmosphere statistics into the model, we make use of periodic Sobolev spaces

$H^s(c_\ell\Omega_T, \gamma_\ell)$, where s denotes a smoothness parameter. The weights γ_ℓ are used to place a higher emphasis on layers on which a strong turbulence is expected, and are assumed to satisfy $\sum_{\ell=1}^L \gamma_\ell = 1$. In practice, they are known quantities derived from previously measured turbulence profiles [42, 48]. Note that this Sobolev-space setting is motivated by a result of Kolmogorov [28], due to which a typical atmospheric turbulence layer is expected to satisfy $s = 11/6$. This assumption is commonly used for both the simulation of atmospheric turbulence profiles [11, 29] as well as in modern reconstruction algorithms for atmospheric tomography; see e.g. [1, 10, 64].

Let $\phi = (\phi_\ell)_{\ell=1,\dots,L}$ denote the turbulence layers, i.e., functions describing the refractive index variations related to temperature fluctuations within the atmosphere at different layers. Then, for given turbulence weights $(\gamma_\ell)_{\ell=1,\dots,L}$ and $0 \leq s \in \mathbb{R}$, the atmospheric tomography operator is defined as [14]

$$A : \prod_{\ell=1}^L H^s(c_\ell\Omega_T, \gamma_\ell) \rightarrow L_2(\Omega_T)^G, \quad \phi = (\phi_\ell)_{\ell=1}^L \mapsto \varphi = ((A_g \phi))_{g=1}^G, \quad (2.1)$$

$$(A_g \phi)(r) := \sum_{\ell=1}^L \phi_\ell(c_\ell r + \alpha_g h_\ell).$$

The operator A , as defined in (2.1), sums up the contributions of each turbulence layer in the direction of the guide stars. Note that so far we considered square domains, while a telescope aperture is typically circular. However, functions known only on the telescope apertures can be extended by zero to the full square via

$$\tilde{\varphi}_g(r) = \begin{cases} \varphi_g(r), & r \in \Omega_A, \\ 0, & r \in \Omega_T \setminus \Omega_A, \end{cases} \quad (2.2)$$

for wavefronts $\varphi_g \in L^2(\Omega_A)$, such that $\tilde{\varphi}_g \in L^2(\Omega_T)$. The effect of this extension was studied in [16], where it was found to produce only very minor errors in the reconstructions along the boundaries of the domain Ω_A . Note that this extension also ensures periodicity, which is therefore no practical restriction of our model.

3 The Singular Value-based Atmospheric Tomography with Fourier Domain Regularization Algorithm

In this section, we recall the SVD for the atmospheric tomography operator A as first proposed in [31] and extended in [23, 60]. Furthermore, we develop the SAFR algorithm and focus on the computational aspects of this method.

3.1 Mathematical description

It is known [23, 31, 60] that the least-squares solution ϕ^\dagger of the equation $A\phi = \varphi$ with A as defined in (2.1) (i.e., LGS-only or NGS-only case) is given by

$$(\phi^\dagger)_\ell(x, y) := \sum_{j,k \in \mathbb{Z}} \left(A_{jk}^\dagger \varphi_{jk} \right)_\ell w_{jk,\ell}^{(s)}(x, y),$$

where

$$\varphi_{jk} = \left(\langle \varphi_g, w_{jk} \rangle_{L_2(\Omega_T)} \right)_{g=1}^G \in \mathbb{C}^G,$$

and A_{jk}^\dagger denotes the pseudo-inverse of the matrix $A_{jk} \in \mathbb{C}^{G \times L}$, which is defined by

$$A_{jk} := \left((2T) w_{jk,\ell}^{(s)}(\alpha_g^x h_\ell, \alpha_g^y h_\ell) \right)_{g,\ell=1}^{G,L}.$$

Here, we use the functions

$$w_{jk,\ell}^{(s)}(x, y) := (1 + \beta_{\ell,T} |(j, k)|^2)^{-s/2} \frac{\gamma_\ell^{1/2}}{c_\ell} w_{jk}((x, y)/c_\ell), \quad \beta_{\ell,T} = \pi^2 (c_\ell T)^{-2},$$

and

$$w_{jk}(x, y) := \frac{1}{2T} e^{i\omega(jx+ky)}, \quad \omega = \frac{\pi}{T},$$

which form orthonormal bases over the spaces $H^s(c_\ell \Omega_T, \gamma_\ell)$ and $L_2(\Omega_T)$, respectively.

Mathematically, the atmospheric tomography problem is ill-posed [9, 40], and thus some form of regularization is required in case of noisy data φ^δ , for which we write

$$\varphi_{jk}^\delta = \left(\langle \varphi_g^\delta, w_{jk} \rangle_{L_2(\Omega_T)} \right)_{g=1}^G. \quad (3.1)$$

For this, consider the SVD of the matrix A_{jk} , i.e., $A_{jk} = U \Sigma V^H$. The inversion of A_{jk} is ill-conditioned [31], and thus, we obtain a regularized inverse of A_{jk} via $\mathcal{R}_\alpha(A_{jk}) = V g_\alpha(\Sigma^T) U^H$, where $g_\alpha : \mathbb{R} \rightarrow \mathbb{R}$ denotes a regularizing filter (cf. [9]) which acts component-wise on the non-zero elements of Σ^T . A regularized solution for the atmospheric tomography problem can then be obtained by

$$(\phi_\alpha^\delta)_\ell(x, y) := \sum_{j,k \in \mathbb{Z}} (\mathcal{R}_\alpha(A_{jk}) \varphi_{jk}^\delta)_\ell w_{jk,\ell}^{(s)}(x, y). \quad (3.2)$$

In order for this approach to approximate the least-squares solution ϕ^\dagger , the filter g_α needs to be chosen appropriately, approaching $s \mapsto 1/s$ as $\alpha \rightarrow 0$. In our numerical experiments, we use a Tikhonov type filter of the form $g_\alpha^{\text{Tikh}}(s) := s/(s^2 + \alpha)$, which generally led to the best performance in our numerical experiments, together with a suitably selected regularization parameter α . Note that throughout our analysis, we used one fixed regularization parameter for the inversion of all matrices A_{jk} . This approach could be further refined by using independent regularization parameters for every matrix A_{jk} . Furthermore, other filter functions or truncation can be used

as well [9]. Note that the practical necessity of truncating the infinite sums in (3.2) at a finite index provides an additional (but by itself in general insufficient) regularization effect in any implementation. Furthermore, note that FEWHA is also based on a specific Tikhonov regularization approach [50].

Finally, note that together with the coefficients

$$b_{jk,\ell} := (1 + \beta_{\ell,T}|(j, k)|^2)^{-s/2} (\mathcal{R}_\alpha(A_{jk})\varphi_{jk}^\delta)_\ell, \quad (3.3)$$

we can equivalently rewrite (3.2) as

$$\begin{aligned} (\phi_\alpha^\delta)_\ell(x, y) &= \sum_{j,k \in \mathbb{Z}} (\mathcal{R}_\alpha(A_{jk})\varphi_{jk}^\delta)_\ell w_{jk,\ell}^{(s)}(x, y) \\ &= \sum_{j,k \in \mathbb{Z}} (1 + \beta_{\ell,T}|(j, k)|^2)^{-s/2} (\mathcal{R}_\alpha(A_{jk})\varphi_{jk}^\delta)_\ell w_{jk,\ell}^{(0)}(x, y) \\ &= \sum_{j,k \in \mathbb{Z}} b_{jk,\ell} w_{jk,\ell}^{(0)}(x, y), \end{aligned} \quad (3.4)$$

which forms the basis of the numerical implementation considered below.

3.2 Numerical Implementation

In order to numerically implement (3.4), we use equidistant grids for discretization on the square domains $c_\ell \Omega_T$ and Ω_T , respectively. This has the advantage that the coefficients φ_{jk}^δ and the outer sums can be efficiently approximated by the two-dimensional (inverse) Discrete Fourier Transform (DFT), which is defined by

$$\text{DFT2}(X)_{j+1,k+1} = \sum_{p,q=0}^{M-1} e^{-2\pi i(jp+kq)/M} X_{p+1,q+1}, \quad \text{for } j, k = 0, \dots, M-1,$$

and

$$\text{IDFT2}(Y)_{p+1,q+1} = \frac{1}{M^2} \sum_{j,k=0}^{M-1} e^{2\pi i(jp+kq)/M} Y_{j+1,k+1}, \quad \text{for } p, q = 0, \dots, M-1,$$

for $X, Y \in \mathbb{C}^{M \times M}$. Note that the DFT2 can be efficiently implemented via the two-dimensional Fast Fourier Transform (**fft2**). For each layer ℓ , we consider a separate grid on the corresponding domains $c_\ell \Omega_T$ and Ω_T with grid points

$$(x_p^\ell, y_q^\ell) = (-c_\ell T + 2c_\ell T \cdot p/M, -c_\ell T + 2c_\ell T \cdot q/M), \quad \text{for } p, q = 0, \dots, M-1,$$

and

$$(x_p, y_q) = (-T + 2T \cdot p/M, -T + 2T \cdot q/M), \quad \text{for } p, q = 0, \dots, M-1.$$

Using this discretization, we obtain

$$w_{jk}(x_p, y_q) = (-1)^{j+k} \frac{1}{2T} e^{2\pi i(jp+kq)/M}, \quad (3.5)$$

and

$$w_{jk,\ell}^{(0)}(x_p^\ell, y_q^\ell) = (-1)^{j+k} \frac{\gamma_\ell^{1/2}}{2c_\ell T} e^{2\pi i (jp+kq)/M}. \quad (3.6)$$

Next, we truncate the infinite sums in (3.4) symmetrically at $\pm m$ with $M = 2m + 1$ (implicitly assuming that M is odd) to obtain

$$(\phi_\alpha^\delta)_\ell(x_p^\ell, y_q^\ell) \approx \sum_{j,k=-m}^m b_{jk,\ell} w_{jk,\ell}^{(0)}(x_p^\ell, y_q^\ell),$$

which, together with the definition

$$n(j) := \begin{cases} j, & j \leq m, \\ j - M, & m < j < M, \end{cases}$$

yields

$$(\phi_\alpha^\delta)_\ell(x_p^\ell, y_q^\ell) \approx \sum_{j,k=0}^{M-1} b_{n(j)n(k),\ell} w_{n(j)n(k),\ell}^{(0)}(x_p^\ell, y_q^\ell). \quad (3.7)$$

Furthermore, due to

$$w_{jk,\ell}^{(0)}(x_p^\ell, y_q^\ell) = w_{(j+r \cdot M)(k+r \cdot M),\ell}^{(0)}(x_p^\ell, y_q^\ell), \quad \forall r \in \mathbb{Z},$$

there holds $w_{n(j)n(k),\ell}(x_p^\ell, y_q^\ell) = w_{jk,\ell}(x_p^\ell, y_q^\ell)$. Hence, together with (3.7) we obtain

$$(\phi_\alpha^\delta)_\ell(x_p^\ell, y_q^\ell) \approx \sum_{j,k=0}^{M-1} b_{n(j)n(k),\ell} w_{jk,\ell}^{(0)}(x_p^\ell, y_q^\ell) \stackrel{(3.6)}{=} \frac{\gamma_\ell^{1/2} M^2}{2c_\ell T} \text{IDFT2}(b_\ell)_{p+1,q+1}, \quad (3.8)$$

with the vector $b_\ell := ((-1)^{j+k} b_{n(j)n(k),\ell})_{j,k=0}^{M-1}$. Similarly, we are able to approximate the coefficient vectors φ_{jk}^δ by

$$\begin{aligned} (\varphi_{n(j)n(k)}^\delta)_g &\stackrel{(3.1)}{=} \langle \varphi_g^\delta, w_{n(j)n(k)} \rangle_{L_2(\Omega_T)} \approx \frac{(2T)^2}{M^2} \sum_{p,q=0}^{M-1} \varphi_g^\delta(x_p, y_q) \bar{w}_{n(j)n(k)}(x_p, y_q) \\ &= \frac{(2T)^2}{M^2} \sum_{p,q=0}^{M-1} \varphi_g^\delta(x_p, y_q) \bar{w}_{j,k}(x_p, y_q) \\ &\stackrel{(3.5)}{=} (-1)^{j+k} \frac{2T}{M^2} \text{DFT2}(\Psi_g^\delta)_{j+1,k+1}, \quad \text{for } g = 1, \dots, G, \end{aligned} \quad (3.9)$$

where the discrete wavefronts are defined as

$$\Psi_g^\delta := (\varphi_g^\delta(x_p, y_q))_{p,q=0}^{M-1} \in \mathbb{R}^{M \times M}.$$

Note that (3.9) amounts to using a right rectangular quadrature rule for the integral in the $L_2(\Omega_T)$ inner product. Now, we define the coefficients

$$b_{jk,\ell g} := \frac{\gamma_\ell^{1/2}}{c_\ell} (1 + \beta_{\ell,T} |(jk)|^2)^{-s/2} (\mathcal{R}_\alpha(A_{jk}))_{\ell g},$$

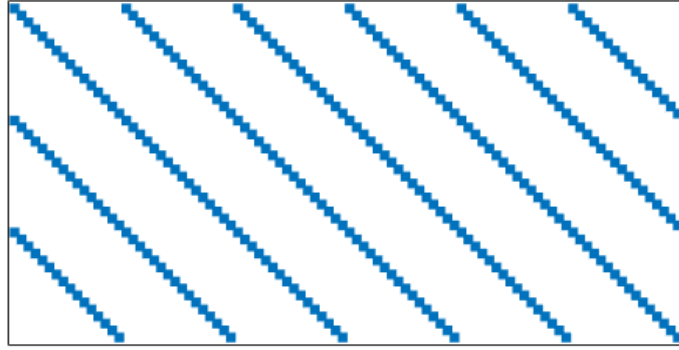


Figure 3.1: Structure of the matrix B , for $L = 3$, $G = 6$.

for which there holds

$$b_{n(j)n(k),\ell} \stackrel{(3.3),(3.9)}{=} (-1)^{j+k} \frac{2c_\ell T}{\gamma_\ell^{1/2} M^2} \sum_{g=1}^G b_{n(j)n(k),\ell g} \cdot \text{DFT2}(\Psi_g^\delta)_{j+1,k+1}. \quad (3.10)$$

Furthermore, we define a sparse matrix $B \in \mathbb{C}^{LM^2 \times GM^2}$ with

$$(B)_{u(j,k,\ell),v(\tilde{j},\tilde{k},g)} = b_{n(j)n(k),\ell g}. \quad (3.11)$$

Here, the one to one mappings

$$\begin{aligned} u(j, k, \ell) &= (\ell - 1) \cdot M^2 + j \cdot M + k + 1, \\ v(\tilde{j}, \tilde{k}, g) &= (g - 1) \cdot M^2 + \tilde{j} \cdot M + \tilde{k} + 1, \end{aligned}$$

are used to convert the three-dimensional indices into linear indices. Note that B is zero on elements with $j \neq \tilde{j}$ or $k \neq \tilde{k}$. In particular, B is non-zero only in LGM^2 of its total LGM^4 entries, see Figure 3.1. Combining (3.8) and (3.10), we now define the SAFR algorithm via its pseudo-code given in Algorithm 1. Its soft real-time computations are given in Algorithm 2. Note that the terms $(-1)^{j+k}$ in the definition of B cancel out within the final algorithm.

Note that the SAFR algorithm can also be interpreted as a certain type of MVM method. To see this, we start by defining the block-diagonal matrices

$$\text{IDFT2}_L := \underbrace{\begin{pmatrix} \text{IDFT2} & & \\ & \ddots & \\ & & \text{IDFT2} \end{pmatrix}}_{L \text{ times}}, \quad \text{DFT2}_G := \underbrace{\begin{pmatrix} \text{DFT2} & & \\ & \ddots & \\ & & \text{DFT2} \end{pmatrix}}_{G \text{ times}},$$

where the blocks $(\text{I})\text{DFT2}$ denote the two-dimensional (inverse) discrete Fourier transform in matrix form. Together with the matrix B given in (3.11), we then obtain a matrix representation of the SAFR Algorithm 1: The reconstructed atmospheric turbulence layers $\Phi^{\alpha,\delta} = (\Phi_\ell^{\alpha,\delta})_{\ell=1}^L$ with $\Phi_\ell^{\alpha,\delta} \in \mathbb{R}^{M \times M}$ can be written as

$$\Phi^{\alpha,\delta} = \text{IDFT2}_L \cdot B \cdot \text{DFT2}_G \cdot \Psi^\delta,$$

where $\Psi^\delta = (\Psi_g^\delta)_{g=1}^G$ is a given wavefront vector with $\Psi_g^\delta \in \mathbb{R}^{M \times M}$.

Algorithm 1 SAFR - Hard real-time computations

Input: $\Psi_1^\delta, \dots, \Psi_G^\delta \in \mathbb{R}^{M \times M}$, B from Algorithm 2; cf. (3.11)

```
1: for  $g = 1, \dots, G$  do
2:    $d_g = \text{fft2}(\Psi_g^\delta)$ 
3: end for
4: for  $j, k = 0, \dots, M - 1, \ell = 1, \dots, L$  do
5:    $(b_\ell)_{j+1,k+1} = \sum_{g=1}^G b_{n(j)n(k),\ell g} \cdot (d_g)_{j+1,k+1}$ 
6: end for
7: for  $\ell = 1, \dots, L$  do
8:    $(\Phi_\alpha^\delta)_\ell = \text{ifft2}(b_\ell)$ 
9: end for
10: return  $(\Phi_\alpha^\delta)_1, \dots, (\Phi_\alpha^\delta)_L \in \mathbb{R}^{M \times M}$ 
```

Algorithm 2 SAFR - Soft real-time computations

Input: $\alpha \in \mathbb{R}^+$, $s \in \mathbb{R}^+$

```
1: for  $j, k = 0, \dots, M - 1$  do
2:    $[U_{n(j)n(k)}, \Sigma_{n(j)n(k)}, V_{n(j)n(k)}] = \text{SVD}(A_{n(j)n(k)})$ 
3:   for  $g = 1, \dots, G, \ell = 1, \dots, L$  do
4:      $b_{n(j)n(k),\ell g} = \frac{\gamma_\ell^{1/2}}{c_\ell} (1 + \beta_{\ell,T} |(n(j), n(k))|^2)^{-s/2}$ 
         $\times \sum_{r=1}^{\text{rank}(A_{n(j)n(k)})} \frac{(\Sigma_{n(j)n(k)})_{r,r}}{(\Sigma_{n(j)n(k)})_{r,r}^2 + \alpha} (\bar{U}_{n(j)n(k)})_{r,g} (V_{n(j)n(k)})_{r,\ell}$ 
5:   end for
6: end for
7: return  $B$  as in (3.11)
```

3.3 The SAFR Algorithm in Three-step AO

The SAFR algorithm is only concerned with the atmospheric tomography step, and is thus independent of the algorithms used for wavefront reconstruction, mirror fitting, and the control strategy. Now, we discuss how we incorporate SAFR in a full AO system, where deformable mirror shapes have to be calculated in every time step. For this, we consider the availability of closed loop Shack-Hartmann (SH) WFS measurement data. Closed loop refers to residual wavefronts, i.e., already corrected with the mirror shapes from the previous time step. Furthermore, in realistic MCAO settings, LGS and NGS are mixed, due to the tip-tilt uncertainty of LGS [17].

However, the SAFR Algorithm itself is only viable for setups where LGS and NGS are not mixed. To still use a three-step method with SAFR in such cases, we use a split tomography approach where NGS are used only for the reconstruction of the tip-tilt component of the atmosphere (referred to as tip-tilt stars (TTS)), while the tip-tilt component from the LGS is completely removed [17]. Then, the TTS and LGS systems can be treated separately by SAFR and, due to the reconstruction of the distinct components, the reconstructed atmospheric turbulence layers can be added. In that case, we denote $G = G_{\text{LGS}} + G_{\text{TTS}}$, such that $(\Psi_1, \dots, \Psi_{G_{\text{LGS}}})$ correspond to wavefronts stemming from LGS and $(\Psi_{G_{\text{LGS}}+1}, \dots, \Psi_G)$ correspond to wavefronts stemming from TTS.

In our numerical experiments, we use a specific three-step AO system, which is shown as pseudo-code in Algorithm 3. We use the CuReD algorithm for wavefront reconstruction and choose the atmospheric turbulence layers such that the mirror fitting step can be omitted. To increase stability and robustness, we use a pseudo open loop control (POLC) approach [8], in which pseudo open loop data is computed from available closed loop measurements. In Algorithm 3, *removeTT* denotes a function which removes the tip-tilt (linear) component of wavefronts, and α_{TT}, B_{TT} denote the regularization parameter and sparse matrix (3.11), respectively, for the atmospheric tomography problem corresponding to the TTS only setting. Note that for the computation of the mirror commands, only the measurements of the previous time step are available. Therefore, the mirror updates will have a 2 time step delay. We use an integrator control, where a predefined gain combines the mirror updates of the last two time steps to increase stability, see line 6 of Algorithm 3.

3.4 Computational Cost

One of the main advantages of the proposed SAFR algorithm is the reduced computational cost as well as reduced memory usage compared to standard MVM methods. We examine the cost of the proposed three-step Algorithm 3 with SAFR against FE-WHA [62, 64] and the COMPASS internal LS-reconstructor (LS).

- **Three-step approach with SAFR:** The computational cost for the three-step method consists of the cost of the computation of pseudo open loop data, wavefront reconstruction via the CuReD, the tip-tilt component removal of LGS wavefronts, the integrator control and atmospheric tomography via SAFR. For $N = M^2$ measurements per guide star, G guide stars and L atmospheric layers, CuReD requires $\mathcal{O}(N)$ Floating Point Operations (FLOPs), while SAFR requires G times the `fft2`, L times the `ifft2` and $L \cdot G \cdot N$ computations for the multiplication of the sparse matrix B in (3.11). Pseudo open loop data is computed by applying the atmospheric tomography operator onto the wavefronts. This is a bilinear interpolation, for which we can leverage the possibility of a matrix free implementation with a cost of $\mathcal{O}(N)$. Note that the domain for the resulting mirror shape updates is predetermined with SAFR to be on an equidistant grid of size N on the domains $[-c_\ell T, c_\ell T]$. In reality, the mirrors might be of different size or spacing, and therefore an

Algorithm 3 Three-step AO with SAFR

Input: i (current time step)

- $s^{(i-1)}$ (measurement vector)
- $c^{(i)}$ (previous mirror commands)
- α (regularization parameter)
- α_{TT} (regularization parameter for TT-reconstruction)
- s (smoothing parameter)
- $gain$ (scalar weight)
- B, B_{TT} (precomputed, sparse matrices in SAFR)

- 1: $(\Psi_1, \dots, \Psi_G) = CuReD(s^{(i-1)})$ ▷ Wavefront reconstruction
- 2: $(\tilde{\Psi}_1, \dots, \tilde{\Psi}_G) = (\Psi_1, \dots, \Psi_G) + A(c^{(i)})$ ▷ POLC
- 3: $(\bar{\Psi}_1, \dots, \bar{\Psi}_{G_{LGS}}) = removeTT(\tilde{\Psi}_1, \dots, \tilde{\Psi}_{G_{LGS}})$ ▷ Tip-Tilt removal for LGS-wavefronts
- 4: $\tilde{\Phi}^{(i+1)} = SAFR(\bar{\Psi}_1, \dots, \bar{\Psi}_{G_{LGS}}, \alpha, s, B) + SAFR(\tilde{\Psi}_{G_{LGS+1}}, \dots, \tilde{\Psi}_G, \alpha_{TT}, s, B_{TT})$ ▷ Atmospheric tomography
- 5: $\Phi^{(i+1)} = (1 - gain) \cdot \Phi^{(i)} + gain \cdot \tilde{\Phi}^{(i+1)}$ ▷ Integrator control
- 6: **return** $\Phi^{(i+1)}$

additional interpolation step is required. The singular systems of the matrices A_{jk} for SAFR can be precomputed in soft-real time and the coefficients can be stored in the matrix B , as defined in (3.11), which amounts to memory storage requirements for a complex matrix of size $N \times LG$.

- **LS reconstructor:** The LS reconstructor computes a control matrix R via singular value decomposition and pseudo-inversion of the interaction matrix (which maps the DM commands a to the sensor measurements s). The reconstruction $R \cdot s^{(i-1)}$ is inserted into the temporal compensator, which is an integrator. The command vector c at time step $i + 1$ is computed as

$$a^{(i+1)} = a^{(i)} + gain \cdot R \cdot s^{(i-1)}. \quad (3.12)$$

Its computational cost is $\mathcal{O}(N^2)$, required for the matrix-vector multiplication. The inversion of the interaction matrix can be pre-computed in soft-real time. Therefore, it additionally requires memory storage for the control matrix of size $NL \times NG$.

- **FEWHA:** FEWHA is an iterative method, in which each iteration is based on the discrete wavelet transform, and which has a computational cost of $\mathcal{O}(N)$. It is based on the CG-method, using a relatively small number of iterations $iter$, typically 2-4. [52].

In general, MVM methods have a computational cost of $\mathcal{O}(N^2)$. Using SAFR, the computational demand is mainly caused by `fft` leading to a reduced complexity of $\mathcal{O}(N \log N)$. In contrast, iterative approaches such as FEWHA or FrIM [53, 54, 55]) yield an asymptotical rate of $\mathcal{O}(N)$. Note that in practice the matrices B in (3.11) and R in (3.12) are pre-computed, thus, their calculation is not included into the hard real-time costs. Due to, e.g., changes of guide star positions or atmospheric conditions, these matrices may have to be recalculated regularly, which is not necessary for iterative methods such as FEWHA or FrIM.

A summary of the computational costs and memory usage associated with all individual components of the considered methods is provided in Table 3.1. The memory usage values therein describe the number of floating point numbers (floats) which have to be stored. The factor 2 in memory usage in Table 3.1 for SAFR stems from the fact that the stored matrix is complex, thus requiring 2 floating point numbers to store one matrix entry. Note that the constant c_1 in the cost of SAFR is expected to be very similar as for one iteration in FEWHA. In particular, the computational costs of SAFR and FEWHA mainly differ in the additional $\mathcal{O}(\log N)$ term, compared to the number of iterations in FEWHA. In the numerical experiments we conduct below, we have WFSs with $N = 74 \times 74$ subapertures. In that specific case, $\log 74^2 \approx 3.7$, which roughly coincides in computational cost with the 2-4 iterations that FEWHA usually takes. Furthermore, SAFR reduces the memory requirements of an MVM method by a factor of N , providing a significant improvement. Note that we did not consider storage necessities for, e.g., method parameters, which are independent of N and can generally be neglected. A precise analysis and comparison of computational cost and memory usage of FEWHA and a general MVM algorithm has been performed in [50].

In terms of real-time computational demands, it is crucial that algorithms are parallelizable and pipelineable. In this regard, SAFR and MVM methods are advantageous, due to their inherent potential for straightforward parallelization and pipelining. For both methods, matrix-vector multiplications are required, which is a highly parallelizable and pipelineable operation. SAFR, in addition, requires the `(i)fft2`, for which parallel and pipelined implementations exist, see e.g. [4, 22, 26]. In contrast, parallelization and pipelining is only a limited possibility for FEWHA, due to its iterative nature [51].

4 Numerical Experiments

In this section, we evaluate the performance of SAFR against FEWHA and the COMPASS internal LS-reconstructor regarding reconstruction quality in numerical experiments. The test setting in this paper is motivated by the instrument MORFEO [3], which is an AO module of the ELT, operating in MCAO. For our numerical simulations, we use the software package COMPASS [12], which in particular allows simulation of all critical sub-components of an AO system in the context of the ELT.

Algorithm	Operation	Computational cost [FLOPs]	memory usage [floats]
SAFR	<code>fft2</code>	$G \cdot \mathcal{O}(N \log N)$	-
	<code>ifft2</code>	$2L \cdot \mathcal{O}(N \log N)$	-
	Computation of elements of B	pre-computed	$2LGN$
	Multiplication with B	$L \cdot G \cdot N$	-
	CuReD	$G \cdot \mathcal{O}(N)$	-
	Tip-tilt removal	$4G_{LGS} \cdot N$	-
	POLC	$L \cdot G \cdot \mathcal{O}(N)$	-
	Interpolation to mirror	$L \cdot \mathcal{O}(N)$	-
	Total cost	$(G + L) \cdot \mathcal{O}(N \log N)$ + $(2L \cdot G + L + 4)\mathcal{O}(N)$ =: $c_1 \mathcal{O}(N \log N)$	$2LGN$
FEWHA	One iteration	$\mathcal{O}(N)$	-
	Total cost	$iter \cdot \mathcal{O}(N)$	-
LS	Inversion of interaction matrix	pre-computed	LGN^2
	Matrix-vector multiplication	$\mathcal{O}(N^2)$	-
	Total cost	$\mathcal{O}(N^2)$	LGN^2

Table 3.1: List of computational and memory cost of all involved computations.

4.1 Test Configuration and Simulation Environment

The AO system configuration is shown in Table 4.1. We simulate a telescope which gathers light through a primary mirror with a 37 m diameter and an 11% central obstruction. The ELT optical design consists of three mirrors denoted by M1, M2, and M3 on-axis with two DMs (M4, M5) for performing the AO correction. For MORFEO, two additional DMs (DM1, DM2) inside the instrument are used for wavefront compensation. Note that we assume the Fried geometry with equidistant actuator spacing for all DMs [13]. Details on the configuration are listed in Table 4.2. We use a 35-layer atmosphere [27] for simulation and reconstruct 3 layers located at the altitudes of the DMs (see Table 4.3) to avoid the mirror fitting step.

In the standard MORFEO setting (Figure 4.1), 6 LGS are positioned in a circle

Parameter	Value
Telescope diameter	37 m
Central obstruction	11%
Na-layer height	90 km
Na-layer FWHM	11.4 km
Field of View	1 arcmin
Evaluation criterion	Strehl ratio
Evaluation wavelength	K band (2200 nm)

	M4	DM1	DM2
Actuators	75×75	47×47	37×37
Altitude	0 km	4 km	12.7 km
Spacing	0.5 m	1 m	1 m

Table 4.2: DM configuration.

Table 4.1: General system parameters for the simulation.

Layer	Altitude	Strength
1	0 m	0.75
2	4000 m	0.15
3	12700 m	0.1

Table 4.3: Layer configuration.

	LGS-WFS	NGS-WFS	TT-WFS
Type	SH WFS	SH WFS	SH WFS
Subap.	74×74	74×74	2×2
Wavelength	589 nm	589 nm	1650 nm

Table 4.4: WFS configuration.

of 90 arcsec diameter. We account for the tip-tilt effect via removing the planar component of LGS wavefronts using 3 faint NGS (TTS) located in a circle of 110 arcsec diameter [17]. We model the sodium layer at which the LGS beam is scattered via a Gaussian random variable with mean altitude $H = 90$ km and FWHM (full width at half maximum) of the sodium density profile of 11.4 km. To each LGS, a SH WFS with 74×74 subapertures is assigned. The faint NGS for tip-tilt removal are equipped with 2×2 SH WFS. The noise induced by the detector read-out is simulated as 3.0 electrons per pixel and frame. For more details see Table 4.4.

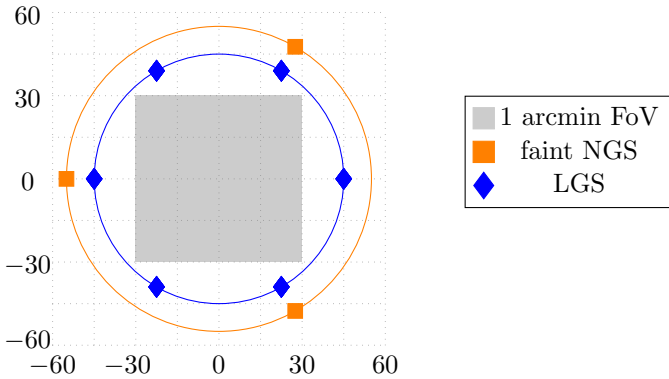


Figure 4.1: Different configurations of faint NGSs (orange) and LGSs (blue). The 1 arcmin FoV is marked in gray.

To validate the reconstruction quality, we use long exposure (LE) and short exposure (SE) Strehl ratio into certain directions [41]. The Strehl ratio is defined as the ratio between the maximum of the real energy distribution of incoming light in the image plane $I(x, y)$ over the hypothetical distribution $I_D(x, y)$, which stems from the assumption of diffraction-limited imaging, i.e.,

$$\text{SR} := \frac{\max_{(x,y)} I(x, y)}{\max_{(x,y)} I_D(x, y)}.$$

By definition, the Strehl ratio is between 0 and 1 and frequently given in percent. A Strehl ratio of 1 means that the influence of the atmosphere has been removed from the observation. For its numerical evaluation, the Marechal criterion is used [41]. We simulate 10000 time steps, corresponding to a 20 seconds interval.

All method specific parameters for SAFR, FEWHA, and the LS algorithm were optimized in COMPASS a-priori. The parameters used in the numerical simulations

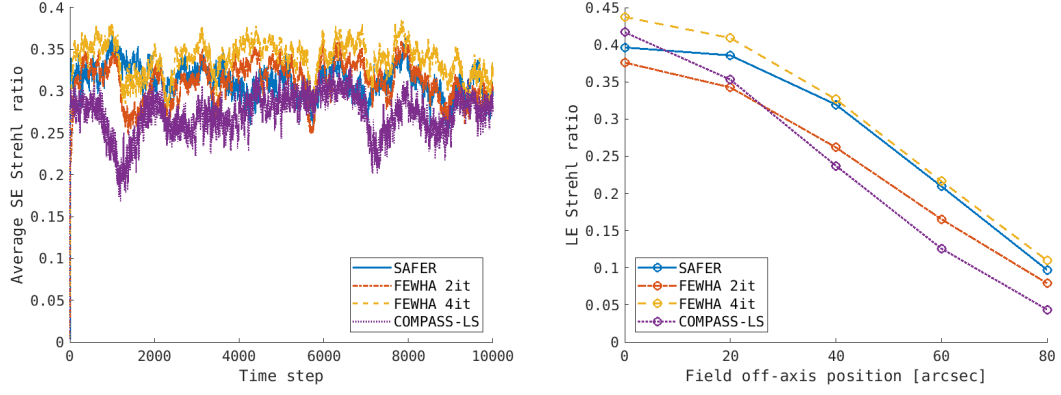
	Parameter	lowflux	highflux
SAFR	α	0.005	0.005
	α_{TT}	0.001	0.01
	s	1.5	1.5
	$gain$	0.5	1
FEWHA	<i>iterations</i>	2-4	2-4
	α	100	250
	α_η	0.2	0.2
	α_J	10^6	10^6
	$gain$	0.6	0.8
LS	$gain$	0.5	0.8

Table 4.5: Method parameters used in the numerical experiments.

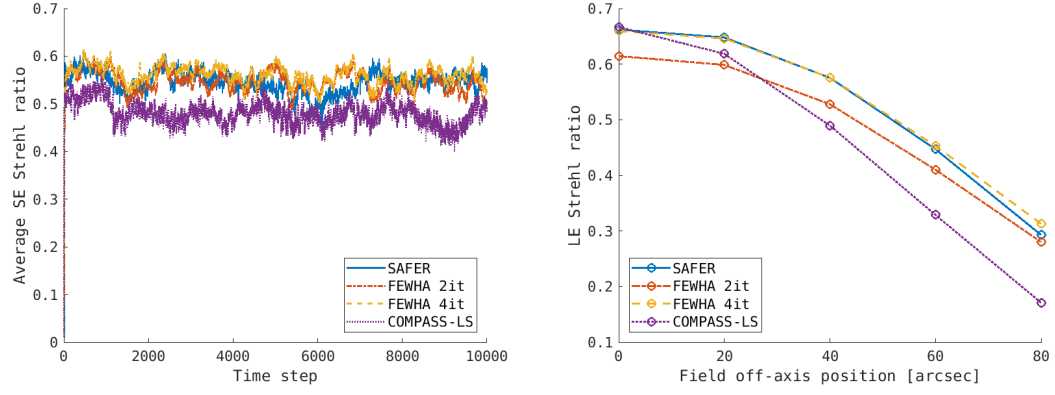
shown in this paper are summarized in Table 4.5, a precise description of the origin and effect of the FEWHA parameters can be found in [52]. For the SAFR Algorithm 1, 2, we used $s = 1.5$ for the smoothing parameter, which is slightly smaller than the choice $s = 11/6$ corresponding to the expected smoothness of a typical atmosphere [28]. This was done to avoid the commonly observed oversmoothing effect inherent in regularization methods with Sobolev norm penalty terms [25, 38].

4.2 Numerical Results

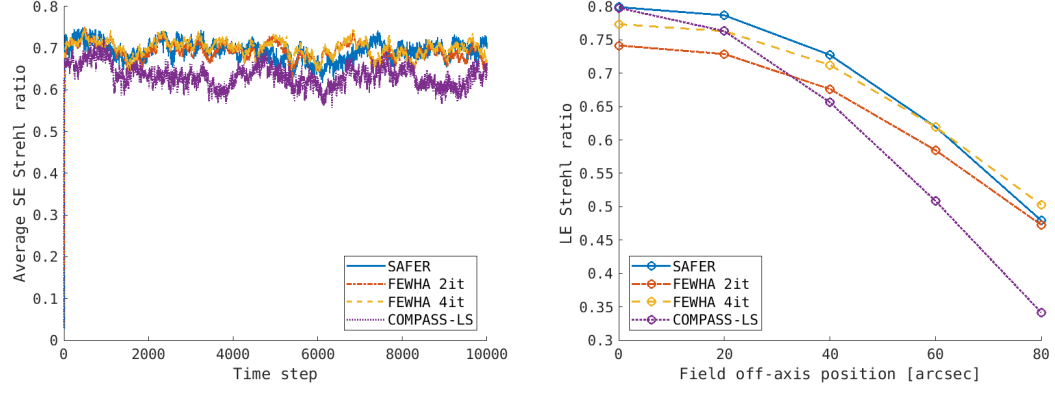
First, we consider a lowflux setting with 500 photons per subaperture per frame, and analyze the performance for different seeing conditions, i.e., for several values of the Fried parameter r_0 . The Fried parameter indicates the medium length of turbulence in the atmosphere, with larger values of r_0 corresponding to better seeing conditions, for which generally better results are expected than for lower values of r_0 . The results are summarized in Figure 4.2. The left plots in Figure 4.2 show the average (over the FoV) SE Strehl ratio over time, while the right plots show the LE Strehl ratio over separation, i.e., distance from the center. We observe that SAFR (blue, solid line) qualitatively outperforms the LS reconstructor (purple, dotted line) in almost every case, with an exception in the very center direction in the $r_0 = 0.097m$ case, i.e., bad seeing conditions in Figure 4.2a. Particularly in outer directions, SAFR yields a much higher LE Strehl ratio than the LS reconstructor. Furthermore, we compared FEWHA with 2 (red, dash-dotted line) and 4 (yellow, dashed line) CG iterations. In [39, 50, 51], it has been shown that the reconstruction quality of FEWHA does not increase significantly for more than 4 iterations. Furthermore, it is worth to note that - with current computational standards - FEWHA with 2 iterations fulfills the real-time requirements of the ELT, while FEWHA with 4 iterations does not. Again, SAFR outperforms FEWHA with 2 iterations in every case and direction, only FEWHA with 4 iterations competes qualitatively with SAFR. For medium seeing conditions ($r_0 = 0.157m$, Figure 4.2b), the LE Strehl is very similar for FEWHA and SAFR. For good seeing conditions ($r_0 = 0.234m$, Figure 4.2c), SAFR



(a) Bad seeing conditions, $r_0 = 0.097 \text{ m}$.



(b) Medium seeing conditions, $r_0 = 0.157 \text{ m}$.



(c) Good seeing conditions, $r_0 = 0.234 \text{ m}$.

Figure 4.2: Average SE Strehl ratio over time (left) and LE Strehl ratio vs. separation (right) after 10,000 time steps for different seeing conditions (different Fried parameter r_0) in the lowflux setting with 500 photons per subaperture per frame.

generally performs better, while FEWHA with 4 iterations performs best for bad seeing conditions ($r_0 = 0.097 \text{ m}$, Figure 4.2a).

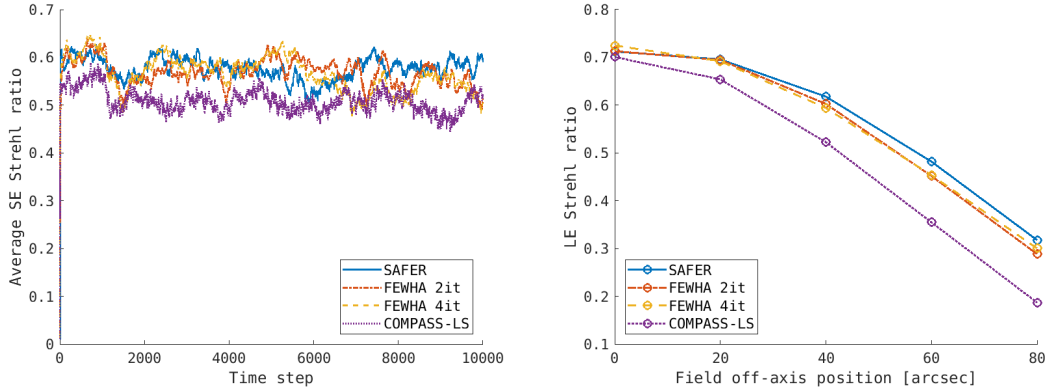


Figure 4.3: Average SE Strehl ratio over time (left) and LE Strehl ratio vs. separation (right) after 10,000 time steps for medium seeing conditions $r_0 = 0.157m$ in the highflux setting with 10,000 photons per subaperture per frame.

For highflux data, i.e., 10,000 photons per subaperture per frame, we only considered the case of medium seeing conditions $r_0 = 0.157m$ in Figure 4.3. Here, the results of the considered methods in terms of LE Strehl ratio are generally closer together, where, again, FEWHA and SAFR outperform the LS reconstructor. Notably, more distant from the center, SAFR performs even better than FEWHA in this case. Finally, note that it is a well-known issue for MCAO systems that the quality of the AO correction degrades further away from the center, see e.g. [40].

5 Conclusion

In this paper, we proposed the SAFR algorithm for the solution of the atmospheric tomography problem, which is part of three-step adaptive optics approaches. We analyzed its computational cost and investigated its performance in an MCAO setting resembling the ELTs MORFEO instrument in numerical simulations. The results obtained within the simulation environment COMPASS showed that in comparison with both the COMPASS internal LS reconstructor and FEWHA, an iterative, matrix-free reconstructor, SAFR qualitatively competes with FEWHA and outperforms the LS reconstructor (an MVM algorithm). In contrast to FEWHA, parallelization and pipelining can be implemented more easily for SAFR, which only relies on standard operations such as matrix multiplication and the discrete Fourier transform. SAFR directly provides a regularized solution to the atmospheric tomography problem without the need for iterations. Furthermore, we found a major improvement with SAFR in terms of both computational expense and memory usage compared to the LS reconstructor in COMPASS. Finally, note that although the analysis of its hard real-time computational complexity showed that SAFR and FEWHA are similar, this does not necessarily imply that this also holds for their actual run-time. While there are efficient implementations of FEWHA on real-time hardware, showing that it meets the requirements for the MORFEO instrument us-

ing 2 iterations [52], a parallelized and pipelined version of SAFR is not yet available and subject of future work.

Acknowledgment

The authors thank Dr. Daniel Jodlbauer for assistance with COMPASS. RR and SH were funded in part by the Austrian Science Fund (FWF) SFB 10.55776/F68 “Tomography Across the Scales”, project F6805-N36 (Tomography in Astronomy). For open access purposes, the authors have applied a CC BY public copyright license to any author-accepted manuscript version arising from this submission. Furthermore, the authors were supported by the NVIDIA Corporation Academic Hardware Grant Program. LW and BS are partially supported by the State of Upper Austria.

References

- [1] G. Auzinger. “New Reconstruction Approaches in Adaptive Optics for Extremely Large Telescopes”. PhD thesis. Johannes Kepler University Linz, 2017.
- [2] M. Davison. “The ill-conditioned nature of the limited angle tomography problem”. In: *SIAM J. Appl. Math.* 43 (1938), pp. 428–448.
- [3] E. Diolaiti et al. “MAORY: A Multi-conjugate Adaptive Optics RelaY for the E-ELT”. In: *Messenger* (2010), 28–9.
- [4] A. El-Khashab and E. Swartzlander. “A modular pipelined implementation of large fast Fourier transforms”. In: *Conference Record of the Thirty-Sixth Asilomar Conference on Signals, Systems and Computers, 2002*. Vol. 2. 2002, 995–999 vol.2. doi: [10.1109/ACSSC.2002.1196933](https://doi.org/10.1109/ACSSC.2002.1196933).
- [5] B. L. Ellerbroeck and C. R. Vogel. “Inverse problems in astronomical optics”. In: *Inverse Problems* 25.6 (2009), p. 063001.
- [6] B. Ellerbroeck, L. Gilles, and C. Vogel. “A Computationally Efficient Wavefront Reconstructor for Simulation or Multi-Conjugate Adaptive Optics on Giant Telescopes”. In: *Proceedings of the SPIE*. Ed. by P. L. Wizinowich and D. Bonaccini. Vol. 4839. Society of Photo-Optical Instrumentation Engineers (SPIE) Conference Series. 2003, pp. 989–1000. doi: [10.1117/12.459673](https://doi.org/10.1117/12.459673).
- [7] B. L. Ellerbroeck, L. Gilles, and C. R. Vogel. “Numerical simulations of multiconjugate adaptive optics wavefront reconstruction on giant telescopes”. In: *Appl. Optics* 42 (2003), pp. 4811–4818.
- [8] B. L. Ellerbroeck and C. R. Vogel. “Simulations of closed-loop wavefront reconstruction for multiconjugate adaptive optics on giant telescopes”. In: *Astronomical Adaptive Optics Systems and Applications*. Ed. by R. K. Tyson and M. Lloyd-Hart. Vol. 5169. International Society for Optics and Photonics. SPIE, 2003, pp. 206 –217. doi: [10.1117/12.506580](https://doi.org/10.1117/12.506580).
- [9] H. W. Engl, M. Hanke, and A. Neubauer. *Regularization of inverse problems*. English. Dordrecht: Kluwer Academic Publishers, 1996, pp. viii + 321. ISBN: 0-7923-4157-0.
- [10] M. Eslitzbichler, C. Pechstein, and R. Ramlau. “An H 1 -Kaczmarz reconstructor for atmospheric tomography”. In: *Journal of Inverse and Ill-Posed Problems* 21 (June 2013). doi: [10.1515/jip-2013-0007](https://doi.org/10.1515/jip-2013-0007).

[11] ESO. *Online description of OCTOPUS*. Tech. rep. Accessed: 2025-03-31. URL: <http://www.eso.org/sci/facilities/develop/ao/tecnico/octopus.html>.

[12] F. Ferreira, D. Gratadour, A. Sevin, and N. Doucet. “COMPASS: An Efficient GPU-based Simulation Software for Adaptive Optics Systems”. In: *2018 International Conference on High Performance Computing and Simulation (HPCS)*. IEEE, July 2018, pp. 180–187. DOI: [10.1109/HPCS.2018.00043](https://doi.org/10.1109/HPCS.2018.00043).

[13] D. L. Fried. “Least-square fitting a wave-front distortion estimate to an array of phase-difference measurements”. In: *J. Opt. Soc. Am.* 67.3 (Mar. 1977), pp. 370–375. DOI: [10.1364/JOSA.67.000370](https://doi.org/10.1364/JOSA.67.000370).

[14] T. Fusco, J.-M. Conan, G. Rousset, L. M. Mugnier, and V. Michau. “Optimal wave-front reconstruction strategies for multi conjugate adaptive optics”. In: *J. Opt. Soc. Am. A* 18 (2001), pp. 2527–2538.

[15] D. T. Gavel. “Tomography for multiconjugate adaptive optics systems using laser guide stars”. In: *Advancements in Adaptive Optics*. Ed. by D. B. Calia, B. L. Ellerbroek, and R. Ragazzoni. Vol. 5490. International Society for Optics and Photonics. SPIE, 2004, pp. 1356–1373. DOI: [10.1117/12.552402](https://doi.org/10.1117/12.552402).

[16] D. Gerth, B. N. Hahn, and R. Ramlau. “The method of the approximate inverse for atmospheric tomography”. In: *Inverse Problems* 31.6 (May 2015), p. 065002. DOI: [10.1088/0266-5611/31/6/065002](https://doi.org/10.1088/0266-5611/31/6/065002).

[17] L. Gilles and B. L. Ellerbroeck. “Split atmospheric tomography using laser and natural guide stars”. In: *J. Opt. Soc. Am.* 25 (2008), pp. 2427–2435.

[18] L. Gilles, B. Ellerbroeck, and C. Vogel. “A comparison of Multigrid V-cycle versus Fourier Domain Preconditioning for Laser Guide Star Atmospheric Tomography”. In: *Adaptive Optics: Analysis and Methods/Computational Optical Sensing and Imaging/Information Photonics/Signal Recovery and Synthesis Topical Meetings on CD-ROM, OSA Technical Digest (CD)*. Optical Society of America, 2007.

[19] L. Gilles, B. Ellerbroeck, and C. Vogel. “Layer-Oriented Multigrid Wavefront Reconstruction Algorithms for Multi-Conjugate Adaptive Optics”. In: *Proceedings of the SPIE*. Ed. by P. L. Wizinowich and D. Bonaccini. Vol. 4839. Society of Photo-Optical Instrumentation Engineers (SPIE) Conference Series. 2003, pp. 1011–1022. DOI: [10.1117/12.459347](https://doi.org/10.1117/12.459347).

[20] L. Gilles, B. L. Ellerbroeck, and C. R. Vogel. “Preconditioned conjugate gradient wavefront reconstructors for multiconjugate adaptive optics”. In: *Applied Optics* 42.26 (2003), pp. 5233–5250.

[21] L. Gilles, C. R. Vogel, and B. L. Ellerbroeck. “Multigrid preconditioned conjugate-gradient method for large-scale wave-front reconstruction”. In: *J. Opt. Soc. Am. A* 19 (2002), pp. 1817–1822.

[22] H. Groginsky and G. Works. “A Pipeline Fast Fourier Transform”. In: *IEEE Transactions on Computers* C-19.11 (1970), pp. 1015–1019. DOI: [10.1109/T-C.1970.222826](https://doi.org/10.1109/T-C.1970.222826).

[23] S. Hubmer and R. Ramlau. “A frame decomposition of the atmospheric tomography operator”. In: *Inverse Problems* 36.9 (2020), p. 094001. DOI: [10.1088/1361-6420/aba4fe](https://doi.org/10.1088/1361-6420/aba4fe).

[24] S. Hubmer and R. Ramlau. “Frame Decompositions of Bounded Linear Operators in Hilbert Spaces with Applications in Tomography”. In: *Inverse Problems* 37.5 (2021), p. 055001. DOI: [10.1088/1361-6420/abe5b8](https://doi.org/10.1088/1361-6420/abe5b8).

[25] S. Hubmer, E. Sherina, and R. Ramlau. “Characterizations of Adjoint Sobolev Embedding Operators with Applications in Inverse Problems”. In: *Electronic Transactions on Numerical Analysis* 59 (2023). Gold OA, pp. 116–144. DOI: [10.1553/etna_v0159s116](https://doi.org/10.1553/etna_v0159s116).

[26] J. Johnston. “Parallel pipeline fast fourier transformer”. In: *IEE Proceedings F (Communications, Radar and Signal Processing)* 130 (6 1983), pp. 564–572. DOI: [10.1049/ip-f-1.1983.0088](https://doi.org/10.1049/ip-f-1.1983.0088).

[27] J. Kolb, H. Gonzalez, C. Juan, and R. Tamai. *Relevant Atmospheric Parameters for E-ELT AO Analysis and Simulations*. ESO-258292 Issue, Technical report ESO, 2015.

[28] A. N. Kolmogorov. *The local structure of turbulence in incompressible viscous fluid for very large reynolds numbers*. In *Dokl. Akad. Nauk SSSR* volume 30, pages 299–303. 1941.

[29] M. Le Louarn, C. Vérinaud, V. Korkiakoski, N. Hubin, and E. Marchetti. “Adaptive optics simulations for the European Extremely Large Telescope”. In: *SPIE Astronomical Telescopes+ Instrumentation*. International Society for Optics and Photonics. 2006, pp. 627234–627234.

[30] F. Natterer. *The Mathematics of Computerized Tomography*. Philadelphia, PA: Society for Industrial and Applied Mathematics, 2001. DOI: [10.1137/1.9780898719284](https://doi.org/10.1137/1.9780898719284).

[31] A. Neubauer and R. Ramlau. “A Singular-Value-Type Decomposition for the Atmospheric Tomography Operator”. In: *SIAM Journal on Applied Mathematics* 77.3 (2017), pp. 838–853. DOI: [10.1137/16M108135X](https://doi.org/10.1137/16M108135X).

[32] M. Poettinger, R. Ramlau, and G. Auzinger. “A new temporal control approach for SCAO systems”. In: *Inverse Problems* 36 (2019), p. 015002.

[33] L. A. Poyneer, D. T. Gavel, and J. M. Brase. “Fast wave-front reconstruction in large adaptive optics systems with use of the Fourier transform”. In: *Journal of the Optical Society of America A* 19.10 (Oct. 2002), p. 2100. ISSN: 1520-8532. DOI: [10.1364/JOSAA.19.002100](https://doi.org/10.1364/JOSAA.19.002100).

[34] F. Quirós-Pacheco, C. Correia, and S. Esposito. “Fourier transform-wavefront reconstruction for the pyramid wavefront sensor”. In: AO4ELT (2010), p. 07005. DOI: [10.1051/ao4elt/201007005](https://doi.org/10.1051/ao4elt/201007005).

[35] S. Raffetseder, R. Ramlau, and M. Yudytskiy. “Optimal mirror deformation for multi conjugate adaptive optics systems”. In: *Inverse Problems* 32.2 (2016), p. 025009. DOI: [10.1088/0266-5611/32/2/025009](https://doi.org/10.1088/0266-5611/32/2/025009).

[36] R. Ramlau, A. Obereder, M. Rosensteiner, and D. Saxenhuber. “Efficient iterative tip/tilt reconstruction for atmospheric tomography”. In: *Inverse Problems in Science and Engineering* 22.8 (2014), pp. 1345–1366. DOI: [10.1080/17415977.2013.873534](https://doi.org/10.1080/17415977.2013.873534).

[37] R. Ramlau and M. Rosensteiner. “An efficient solution to the atmospheric turbulence tomography problem using Kaczmarz iteration”. In: *Inverse Problems* 28 (2012), p. 095004.

[38] R. Ramlau and G. Teschke. “Regularization of Sobolev Embedding Operators and Applications to Medical Imaging and Meteorological Data. Part I: Regularization of Sobolev Embedding Operators”. In: *Sampling Theory in Signal and Image Processing* 3.2 (2004), pp. 175–195.

[39] R. Ramlau and B. Stadler. “An augmented wavelet reconstructor for atmospheric tomography”. In: *Electron. Trans. Numer. Anal.* 54 (2021), pp. 256–275. DOI: [10.1553/etna_v0154s256](https://doi.org/10.1553/etna_v0154s256).

[40] R. Ramlau and B. Stadler. “On some analytic properties of the atmospheric tomography operator: Non-Uniqueness and reconstructability issues”. In: *Inverse Problems and Imaging* 19.4 (2025), pp. 715–733. ISSN: 1930-8345. DOI: [10.3934/ipi.2024051](https://doi.org/10.3934/ipi.2024051).

[41] F. Roddier. *Adaptive Optics in Astronomy*. Cambridge University Press, 1999.

[42] F. Roddier. “V The Effects of Atmospheric Turbulence in Optical Astronomy”. In: ed. by E. Wolf. Vol. 19. *Progress in Optics*. Elsevier, 1981, pp. 281–376. DOI: [https://doi.org/10.1016/S0079-6638\(08\)70204-X](https://doi.org/10.1016/S0079-6638(08)70204-X).

[43] M. Rosensteiner. “Cumulative Reconstructor: fast wavefront reconstruction algorithm for Extremely Large Telescopes”. In: *J. Opt. Soc. Am. A* 28 (2011), pp. 2132–2138.

[44] M. Rosensteiner. “Wavefront reconstruction for extremely large telescopes via CuRe with domain decomposition”. In: *J. Opt. Soc. Am. A* 29 (2012), pp. 2328–2336.

[45] M. Rosensteiner and R. Ramlau. “The Kaczmarz algorithm for multi-conjugate adaptive optics with laser guide stars”. In: *J. Opt. Soc. Am. A* 30 (2013), pp. 1680–1686.

[46] D. Saxenhuber. “Gradient-based reconstruction algorithms for atmospheric tomography in Adaptive Optics systems for Extremely Large Telescopes”. 2016.

[47] D. Saxenhuber and R. Ramlau. “A Gradient-based method for atmospheric tomography”. In: *Inverse Problems and Imaging* 10.3 (2016), pp. 781–805. DOI: 10.3934/ipi.2016022.

[48] D. Saxenhuber, G. Auzinger, M. L. Louarn, and T. Helin. “Comparison of methods for the reduction of reconstructed layers in atmospheric tomography”. In: *Appl. Opt.* 56.10 (Apr. 2017), pp. 2621–2629. DOI: 10.1364/AO.56.002621.

[49] I. Shatokhina, A. Obereder, M. Rosensteiner, and R. Ramlau. “Preprocessed cumulative reconstructor with domain decomposition: a fast wavefront reconstruction method for pyramid wavefront sensor”. In: *Applied Optics* 52.12 (Apr. 2013), p. 2640. ISSN: 2155-3165. DOI: 10.1364/AO.52.002640.

[50] B. Stadler. “Real-time computing methods for astronomical adaptive optics”. PhD thesis. Johannes Kepler Universität Linz, 2021.

[51] B. Stadler, R. Biasi, M. Manetti, and R. Ramlau. “Parallel implementation of an iterative solver for atmospheric tomography”. In: *2021 21st International Conference on Computational Science and Its Applications (ICCSA)*. 2021, pp. 123–132. DOI: 10.1109/ICCSA54496.2021.00026.

[52] B. Stadler and R. Ramlau. “Performance of an iterative wavelet reconstructor for the Multi-conjugate Adaptive Optics RelaY of the Extremely Large Telescope”. In: *Journal of Astronomical Telescopes, Instruments, and Systems* 8.2 (2022), p. 021503. DOI: 10.1117/1.JATIS.8.2.021503.

[53] M. Tallon et al. “Fractal iterative method for fast atmospheric tomography on extremely large telescopes”. In: *Adaptive Optics Systems II, no. 7736 in Proc. SPIE*. 2010, pp. 77360X–77360X–10.

[54] M. Tallon et al. “Performances of MCAO on the E-ELT using the fractal iterative method for fast atmospheric tomography”. In: *Second International Conference on Adaptive Optics for Extremely Large Telescopes*. 2011, p. 63.

[55] E. Thiébaut and M. Tallon. “Fast minimum variance wavefront reconstruction for extremely large telescopes”. In: *J. opt. Soc. Am. A* 27 (2010), pp. 1046–1059.

[56] A. Tokovinin, M. L. Louarn, and M. Sarazin. “Isoplanatism in a multiconjugate adaptive optics system”. In: *J. Opt. Soc. Am. A* 17.10 (2000), pp. 1819–1827. DOI: 10.1364/JOSAA.17.001819.

[57] C. Vogel and Q. Yang. “Fast optimal wavefront reconstruction for multi-conjugate adaptive optics using the Fourier domain preconditioned conjugate gradient algorithm”. In: *Optics Express* 15 (2006), pp. 7487–7498.

[58] C. R. Vogel and Q. Yang. “Multigrid algorithm for least-squares wavefront reconstruction”. In: *Applied Optics* 45.4 (Feb. 2006), p. 705. ISSN: 1539-4522. DOI: 10.1364/AO.45.000705.

[59] L. Weissinger. “Realization of the Frame Decomposition of the Atmospheric Tomography Operator”. MA thesis. JKU Linz, 2021. URL: https://lissss.jku.at/permalink/f/n2r1to/ULI_alma5185824070003340.

- [60] L. Weissinger, S. Hubmer, B. Stadler, and R. Ramlau. “Singular value and frame decomposition-based reconstruction for atmospheric tomography”. In: *Inverse Problems on Large Scales*. Ed. by B. Mejri, R. Ramlau, and O. Scherzer. Berlin, Boston: De Gruyter, 2025, pp. 151–180. ISBN: 9783111357270. DOI: [doi:10.1515/9783111357270-008](https://doi.org/10.1515/9783111357270-008).
- [61] Q. Yang, C. R. Vogel, and B. L. Ellerbroek. “Fourier domain preconditioned conjugate gradient algorithm for atmospheric tomography”. In: *Appl. Optics* 45 (2006), pp. 5281–5293.
- [62] M. Yudytskiy. “Wavelet methods in adaptive optics”. PhD thesis. Johannes Kepler University Linz, Austria, 2014.
- [63] M. Yudytskiy, T. Helin, and R. Ramlau. “A frequency dependent preconditioned wavelet method for atmospheric tomography”. In: *Proceedings of the Third AO4ELT Conference, S. Esposito and L. Fini, eds., Firenze*. 2013. DOI: [10.12839/AO4ELT3.13433](https://doi.org/10.12839/AO4ELT3.13433).
- [64] M. Yudytskiy, T. Helin, and R. Ramlau. “Finite element-wavelet hybrid algorithm for atmospheric tomography”. In: *J. Opt. Soc. Am. A* 31 (2014), pp. 550–560.